

Oxygen Transport Ceramic Membranes

Quarterly Report

October- December 2002

By:

Dr. Sukumar Bandopadhyay
and
Dr. Nagendra Nagabhushana

**School of Mineral Engineering
University of Alaska Fairbanks**

Issued: January 2003

DOE Award # DE-FC26-99FT400054

University of Alaska Fairbanks
School of Mineral Engineering
Duckering 355
Fairbanks, AK 99775

Table of Contents

Abstract		iii
Disclaimer		iv
Executive Summary		v
Task 1.	Development of Ceramic Membrane/Metal Joints	1
Task 2.	Determine material mechanical properties under conditions of high temperature and reactive atmosphere	5
Task 3.	Preparation and Characterization of Dense Ceramic oxygen Permeable Membranes	8
Task 4.	Assessment of Microstructure of the Membrane Materials to Evaluate the Effects of vacancy-Impurity Association, defect Clusters, and Vacancy Dopant Association on the Membrane Performance and Stability	17
Task 5.	Measurement of Surface Activation/Reaction rates in Ion Transport Membranes using Isotope Tracer and Transient Kinetic Techniques	18
Project Milestone log		33
Project Status Report		35

ABSTRACT

In the present quarter, experiments are presented on ceramic/metal interactions of Zirconia/ Ni-B-Si system and with a thin Ti coating deposited on zirconia surface. Processing of perovskites of LSC, LSF and LSCF composition for evaluation of mechanical properties as a function of environment are begun. The studies are to be in parallel with LSFCO composition to characterize the segregation of cations and slow crack growth in environmental conditions. $\text{La}_{1-x}\text{Sr}_x\text{FeO}_{3-d}$ has also been characterized for paramagnetic ordering at room temperature and the evolution of magnetic moments as a function of temperature are investigated. Investigation on the thermodynamic properties of the membrane materials are continued to develop a complete model for the membrane transport.

DISCLAIMER

This report was prepared as an account of work sponsored by an agency of the United States Government. Neither the United States Government nor any agency thereof, nor any of their employees, makes any warrantee, express or implied, or assumes any legal liability or responsibility for the accuracy, completeness, or usefulness of any information, apparatus, product, or process disclosed, or represents that its use would not infringe privately owned rights. Reference herein to any specific commercial product, process, or service by trade name, trademark, manufacturer, or otherwise does not necessarily constitute or imply its endorsement, recommendation, or favoring by the United States Government or any agency thereof. The views and opinions of the authors expressed herein do not necessarily state or reflect those of the United States Government or any agency thereof.

Executive Summary

Conversion of natural gas to liquid fuels and chemicals is a major goal for the Nation as it enters the 21st Century. Technically robust and economically viable processes are needed to capture the value of the vast reserves of natural gas on Alaska's North Slope, and wean the Nation from dependence on foreign petroleum sources. Technologies that are emerging to fulfill this need are all based syngas as an intermediate. Syngas (a mixture of hydrogen and carbon monoxide) is a fundamental building block from which chemicals and fuels can be derived. Lower cost syngas translates directly into more cost-competitive fuels and chemicals.

The currently practiced commercial technology for making syngas is either steam methane reforming (SMR) or a two-step process involving cryogenic oxygen separation followed by natural gas partial oxidation (POX). These high-energy, capital-intensive processes do not always produce syngas at a cost that makes its derivatives competitive with current petroleum-based fuels and chemicals.

In the mid 80's BP invented a radically new technology concept that will have a major economic and energy efficiency impact on the conversion of natural gas to liquid fuels, hydrogen, and chemicals.¹ This technology, called Electropox, integrates oxygen separation with the oxidation and steam reforming of natural gas into a single process to produce syngas with an economic advantage of 30 to 50 percent over conventional technologies.²

The Electropox process uses novel and proprietary solid metal oxide ceramic oxygen transport membranes [OTMs], which selectively conduct both oxide ions and electrons through their lattice structure at elevated temperatures.³ Under the influence of an oxygen partial pressure

¹Mazanec, T. J.; Cable, T. L.; Frye, J. G., Jr.; US 4,793,904, 27 Dec **1988**, assigned to The Standard Oil Company (now BP America), Mazanec, T. J.; Cable, T. L.; US 4,802,958, 7 Feb **1989**, assigned to the Standard Oil Co. (now BP America), Cable, T. L.; Mazanec, T. J.; Frye, J. G., Jr.; European Patent Application 0399833, 24 May **1990**, published 28 November **1990**.

²Bredesen, R.; Sogge, J.; "A Technical and Economic Assessment of Membrane Reactors for Hydrogen and Syngas Production" presented at Seminar on the Ecol. Applic. of Innovative Membrane Technology in the Chemical Industry", Cetraro, Calabria, Italy, 1-4 May **1996**.

³Mazanec, T.J., *Interface*, **1996**; Mazanec, T.J., *Solid State Ionics*, 70/71, **1994** 11-19; "Electropox: BP's Novel Oxidation Technology", T.J. Mazanec, pp 212-225, in "The Role of Oxygen in Improving Chemical Processes", M. Fetizon and W.J. Thomas, eds, Royal Society of Chemistry, London, **1993**; "Electropox: BP's Novel Oxidation Technology", T.J. Mazanec, pp 85-96, in "The Activation of Dioxygen and Homogeneous Catalytic Oxidation", D.H.R. Barton, A. E. Martell, D.T. Sawyer, eds, Plenum Press, New York, **1993**; "Electrocatalytic Cells for

gradient, oxygen ions move through the dense, nonporous membrane lattice at high rates with 100 percent selectivity. Transported oxygen reacts with natural gas on the fuel side of the ceramic membrane in the presence of a catalyst to produce syngas.

In 1997 BP entered into an OTM Alliance with Praxair, Amoco, Statoil and Sasol to advance the Electropox technology in an industrially sponsored development program. These five companies have been joined by Phillips Petroleum and now are carrying out a multi-year \$40+ million program to develop and commercialize the technology. The program targets materials, manufacturing and engineering development issues and culminates in the operation of semi-works and demonstration scale prototype units.

The Electropox process represents a truly revolutionary technology for conversion of natural gas to synthesis gas not only because it combines the three separate unit operations of oxygen separation, methane oxidation and methane steam reforming into a single step, but also because it employs a chemically active ceramic material in a fundamentally new way. On numerous fronts the commercialization of Electropox demands solutions to problems that have never before been accomplished. Basic problems in materials and catalysts, membrane fabrication, model development, and reactor engineering all need solutions to achieve commercial success.

Six important issues have been selected as needing understanding on a fundamental level at which the applied Alliance program cannot achieve the breadth and depth of understanding needed for rapid advancement. These issues include

1. Oxygen diffusion kinetics (University of Houston)
2. Grain structure and atomic segregation (University of Illinois - Chicago)
3. Phase stability and stress development (University of Missouri - Rolla)
4. Mechanical property evaluation in thermal and chemical stress fields (University of Alaska Fairbanks)
5. Graded ceramic/metal seals (Massachusetts Institute of Technology)

Statement of Work

Chemical Reaction", T.J. Mazanec, T.L. Cable, J.G. Frye, Jr.; Prep Petrol Div ACS, San Fran, **1992** 37, 135-146; T.J. Mazanec, T.L. Cable, J.G. Frye, Jr.; *Solid State Ionics*, **1992**, 53-56, 111-118.

- Task 1 Design, fabricate and evaluate ceramic to metal seals based on graded ceramic powder / metal braze joints.
- Task 2 Determine materials mechanical properties under conditions of high temperatures and reactive atmospheres.
- Task 3 Evaluate phase stability and thermal expansion of candidate perovskite membranes and develop techniques to support these materials on porous metal structures.
- Task 4 Assess the microstructure of membrane materials to evaluate the effects of vacancy-impurity association, defect clusters, and vacancy-dopant association on the membrane performance and stability.
- Task 5 Measure kinetics of oxygen uptake and transport in ceramic membrane materials under commercially relevant conditions using isotope labeling techniques.

Task 1

Development of Ceramic Membrane/Metal Joints

**Prof. Thomas W. Eagar, Dr Harold R Larson,
Mr Raymundo Arroyave and Ms Jocelyn L. Wiese**

ABSTRACT

The possibility of using more complex interfacial engineering approaches to the development of reliable and stable perovskite/metal seals is discussed. Experiments are presented and ceramic/metal interactions are characterized. Future work regarding this approach is proposed.

We determined that it was necessary to find other options, probably more complex, in order to prevent this excessive reaction between the perovskite and the braze. By limiting the extent of this reaction, the mechanical integrity of the membrane would not be compromised and the reliability of the entire system would also be improved. Figure 4 presents the concept that we have been exploring so far:

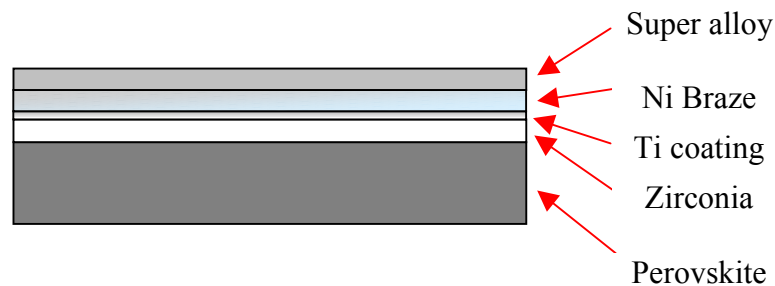


Figure 1 Interfacial Modification of Perovskite Membranes

Figure 1 depicts a rather complex interfacial structure that could allow the formation of a strong, stable interface between a perovskite ceramic and a nickel-based super alloy:

Based on the recent progress by the University of Missouri-Rolla regarding the deposition of ceramic coatings on perovskite substrates it is believed that a ceramic oxide such as ceria or zirconia-based coating could be used as an effective diffusion barrier to prevent excessive interaction between the braze and the perovskite membrane.

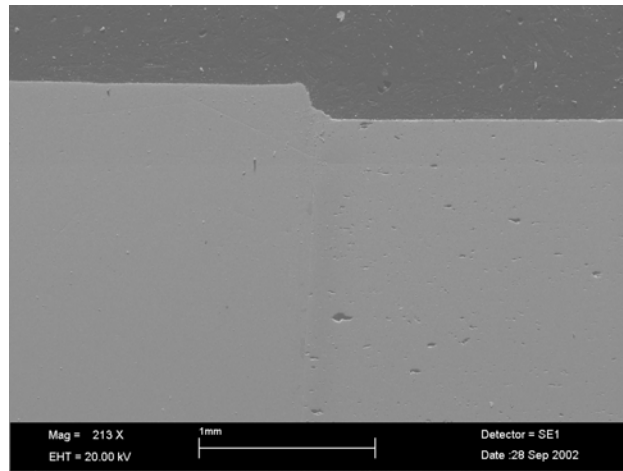


Figure 2 Zirconia/Inconel Joint: Use of active coating and Ni-based super alloy

Stable ceramics such as ceria or zirconia have the problem that, due to their relatively low surface energy, they do not tend to be wetted by molten metals, such as Ni-based braze alloys. A further processing of such composite interfaces is thus needed to promote wetting. One option is the use of active coatings (materials with high oxygen affinity) that promote the formation of a stable interface between the ceramic substrate and the Ni-braze.

Figure 2 depicts a zirconia/Ni-based super alloy joint created using the process described above: A relatively thin Ti coating was deposited on top of the zirconia substrate and a Ni-based amorphous foil was placed between the coated zirconia sample and the Ni-based super alloy. The process was designed so at a relatively high temperature, the Ti coating would react with the zirconia and produce a Ti-based oxide that could in turn be wetted by the Ni-braze. Oxygen vacancies were created within the zirconia lattice and oxygen migration was promoted due to the large oxygen potential gradient across the zirconia/Ti interface. Once the Ti-oxide layer was formed, the joint was heated up until the solidus-liquidus two-phase region of the Ni-based braze alloy was reached. The liquid wetted the Ti oxide and a stable interface between the Ti-O coating and the Ni-based was created. As can be seen from the figure above, no interfacial defects were observed at the joint.

One of the advantages of using Ni-based brazing alloys is the fact that this alloy system usually uses both Si and B as melting point depressants. This means that in theory, it is possible to create the joint at one temperature and then let Diffusional processes drive the melting point depressants out of the Ni-based interlayer and into the base materials (in this case the Ni-based super alloy). Since B is a fast diffusant and has the greatest effect regarding the depression of the liquidus surface in the Ni-B-Si system, it is expected that by heat-treating the joint at temperatures comparable to the joining temperature it is possible to achieve isothermal solidification of the interface. This implies that the actual maximum operating temperature of the joint could be higher than the joining temperature.

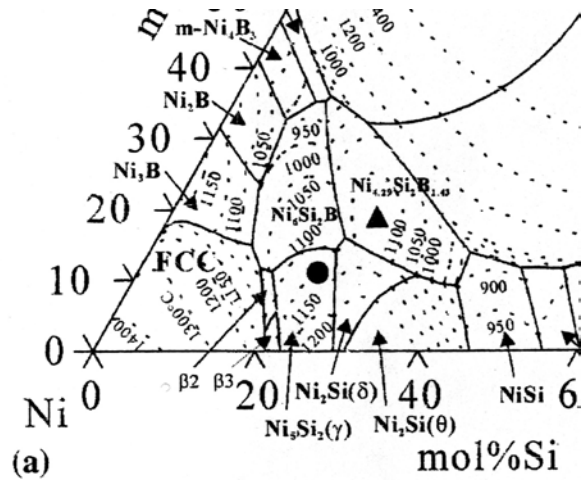


Figure 3 Ni-B-Si Ternary System: Liquidus Surface

Figure 3 illustrates the primary surface of solidification for the Ni-B-Si system. The Ni brazes being used in this project lie at the Ni-rich corner of the diagram, and from the figure it can be seen how the liquidus surface descends with a great slope as the amount of Si and B increase.

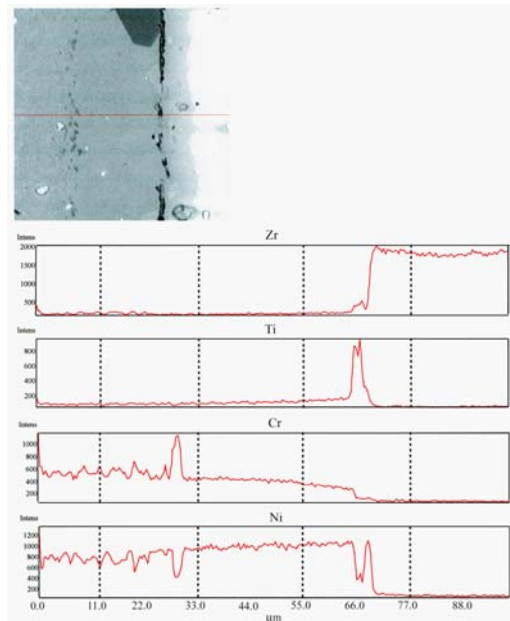


Figure 4 Compositional Profiles across Zirconia/Ni-braze Interface

Figure 4 illustrates the compositional profile across the Zirconia/Ni braze interface. It can be seen how Zr is being dissolved into the braze, which can be explained by a localized transformation of the zirconia lattice into zirconia + Zr metal, plus a very negative Gibbs free energy of dilution of Zr in a Ni-based liquid alloy. From the figure, the Ti peak is a clear proof of the relative stability of the Ti-O coating against further dissolution by the Ni-based braze. The Cr-profile illustrates the further Cr enrichment of the braze alloy, which in turn would have great effects on the overall oxidation resistance of the braze.

We are currently working on obtaining concentric zirconia/metal seals using Ni-based brazing alloys. We set-up an inert-atmosphere furnace and have already coated with a thin film of Ti metal on several zirconia tubes. The tubes will be brazed to Inconel and Haynes 230 fabricated tubes and the resulting seals will be evaluated and analyzed.

The following activities are expected to be completed:

1. Creation of concentric brazed joints.

Brazes will be created using the techniques developed so far. The geometric aspect ratio between overlap distance and joint diameter will be kept at 1/1, since according to previous Finite Element calculations, this constitutes the optimum ratio.

2. Evaluation of sealing capabilities.

The integrity of the concentric seals will be evaluated and the resulting interfaces will be examined to determine the degree of integrity resulting from the proposed joining techniques.

3. Studies of Thermal Stability of Interfaces

The joints will be subjected to prolonged periods at relatively high temperatures to determine the conditions under which the joints' sealing capabilities degrade

TASK 2: Determine material mechanical properties under conditions of high temperature and reactive atmosphere

Prof. Sukumar Bandopadhyay and Dr. Nagendra Nagabhushana

University of Alaska Fairbanks

INTRODUCTION

In earlier reports, we have reported on the strength of OTM tubes tested in C-ring geometry. For the third year, emphasis was also laid on evaluating the strength of membranes in a flexure geometry. In Accordance, 4 –point bend fixture were designed and fabricated. In the last project meeting at University of Missouri-Rolla, it was decided to look at the slow –crack growth behavior of the materials as a function of environment. However, due to lack of requisite samples, initial studies are done on Lanthanum Strontium Cobaltite and Lanthanum Strontium Ferrite.

EXPERIMENTAL PROCEDURE

Perovskites of the composition listed in Table 1, were acquired from Praxair Specialty Ceramics. The materials were processed by combustion spray pyrolysis. The average particle size ‘ d_{50} ’ was 0.6 μm . The materials were analyzed by X-ray to determine the lattice structure.

Green samples of dimension 50 x 6.7x 10 mm were fabricated by mixing with PVA as binder and cold pressing in a steel die at pressure of 28 MPa. The samples are to be sintered at 1350°C for 2-3 hours to the final density of ~ 90-95%.

The samples processed will be evaluated for strength and characterized for crack growth in the environment. For this studies will be done fixture b depicted in Figure 5.

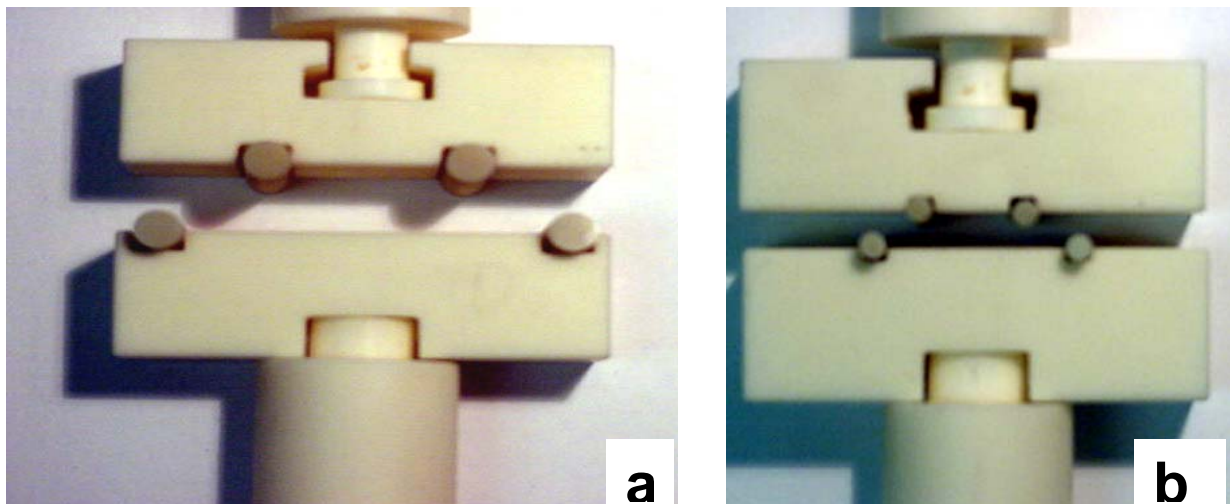


Figure 5: Fixtures designed for 4-Point flexure testing of LSFCE bars

Table 1: Composition of perovskite to be processed for flexure tests.

No.	Composition	Particle size d_{50}	Major Phase
1	LaSrFeO	0.6	Perovskite
2	La _{0.8} Sr _{0.8} Co	0.6	Perovskite
3	La _{0.2} Sr _{0.8} Co _{0.8} Fe _{0.2}	0.6	Perovskite
4	La _{0.6} Sr _{0.4} Co _{0.2} Fe _{0.8}	0.6	Perovskite
5	La _{0.8} Sr _{0.2} Co _{0.8} Fe _{0.2}	0.6	Perovskite

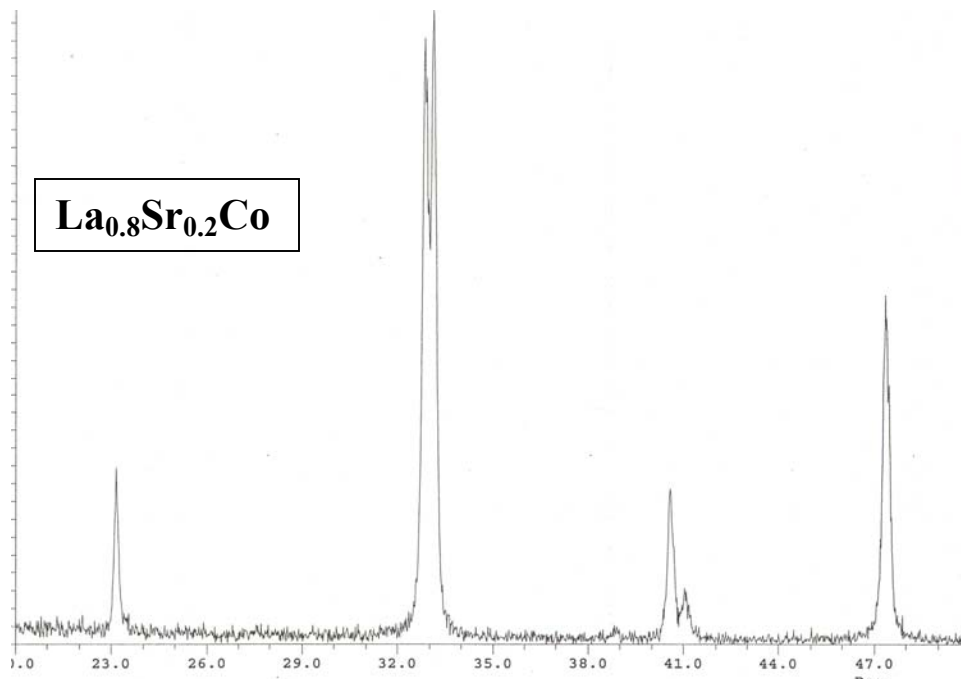


Figure 6a XRD analysis of La_{0.8}Sr_{0.2}Co perovskite

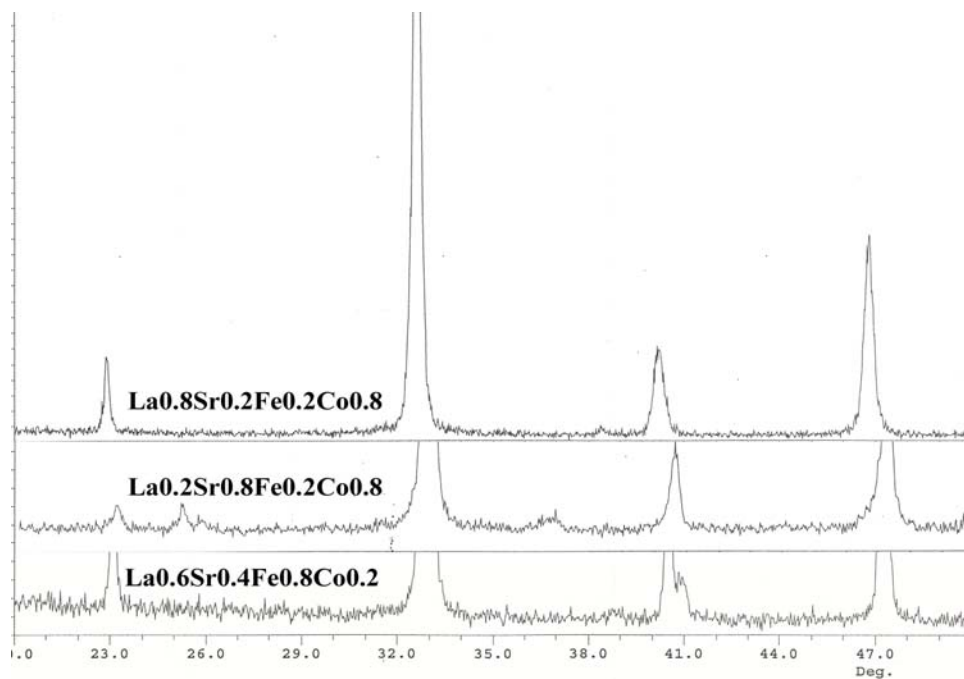


Figure 6b XRD analysis of LSCF perovskites

The sample will be analyzed in a XRD after sintering and characterized for porosity and final density before proceeding to mechanical strength as a function of environment.

Previous studies on LSFCEO membranes have indicated preferential segregation of cations upon exposure to environment and stress. Studies on the well characterized LSCF in terms of defect chemistry and stability would provide an excellent point of study for comparison.

Task 3: Preparation and Characterization of Dense Ceramic oxygen Permeable Membranes

**By: Professor Harlan Anderson, University of Missouri-Rolla
Dr. Wayne Huebner, Dr. Xiao-Dong Zhou**

INTRODUCTION*

The perovskite-type oxides encompass a large variety of chemical compositions that contribute to their diverse and unique properties. Of them, $\text{La}_{1-x}\text{Sr}_x\text{FeO}_{3-\delta}$ is of particular interest in the applications of gas separation membrane, mixed ionic and electronic conductors and solid oxide fuel cells because of their special structural, electric and magnetic properties. Dann et al.¹ have reported the orthorhombic phase for $0 \leq x \leq 0.2$, the rhombohedral phase for $0.4 \leq x \leq 0.7$ and the cubic phase for $0.8 \leq x \leq 1.0$. Néel temperatures of this series compounds were measured by Shimony et al.² with values from 750K to about 100K as x changes from 0 to 1 and around 300K when $x = 0.4$.

$\text{La}_{1/3}\text{Sr}_{2/3}\text{FeO}_3$ has paramagnetic ordering at room temperature, with an average charge +3.67 at each Fe site. At low temperature, anti-ferromagnetic ordering with a partial ordering valence-state was first reported by Battle³, which showed that the charge ordering state took place at $T \leq 189\text{K}$. The ordering state was described as $(+\text{Fe}^{+5})(+\text{Fe}^{+3})(-\text{Fe}^{+3})(-\text{Fe}^{+5})(-\text{Fe}^{+3})(+\text{Fe}^{+3})\dots$ along the body diagonal (1,1,1) with respect to the ideal perovskite structure, where the sign in front of Fe indicates the orientation of magnetic moments. At 50 K, the moments were $3.6 \mu_B$ for Fe^{3+} , and $2.7 \mu_B$ for Fe^{5+} . It is interesting to investigate the evolution of magnetic moments as a function of temperature.

Experimental

The Pechini method^{4,5} was used to synthesize nanocrystalline particles, in this process a polymeric solution was formed due to a chelating reaction between cations and chelants. Mössbauer spectroscopy and neutron diffraction were performed at room temperature on the sintered and quenched specimens. During the quenching experiments, the specimens were first heated at 1000°C with a flowing gas atmosphere of N_2 , air, or CO/CO_2 mixtures for 24 hours, and then quenched to room temperature. For Neutron Diffraction (ND) studies, samples were contained in 3 mm V metal cells and data were collected at 1.4785 \AA over a range of 5° - 105° (2θ). One gram powder was used for neutron measurement at temperatures from 15K to 200K on the PSD at MURR. The neutron data show that all peaks are sharp, which indicates the sample is homogenous. All peaks, except three peaks at 6.38° , 19.17° and 26.50° , can be indexed by the unit cell $a=5.17$, $c=13.36$ in space group $R\bar{3}c$ in the hexagonal setting. The remaining peaks can be indexed by using the same cell but in space group $R\bar{3}c$. Rietveld refinement was carried out using the FULLPROF code, in which the magnetic ordering was taken into account because of the sensitivity of neutron diffraction to the magnetic ordering of the Fe atoms.

* This is a manuscript draft version we will submit for publishing with the co-authors as Z. Chu, W. B. Yelon, J. Yang, W. J. James, and Q. Cai.

RESULTS AND DISCUSSIONS

The intensities of these two peaks decrease as the temperature increases. They completely disappear at a temperature between 186K and 194K. This is consistent with the transition temperature 189K^3 , which is also confirmed by magnetic measurement (Figure 7). The Neel temperature of the compound is about 180 K, which is a response to the charge ordering.

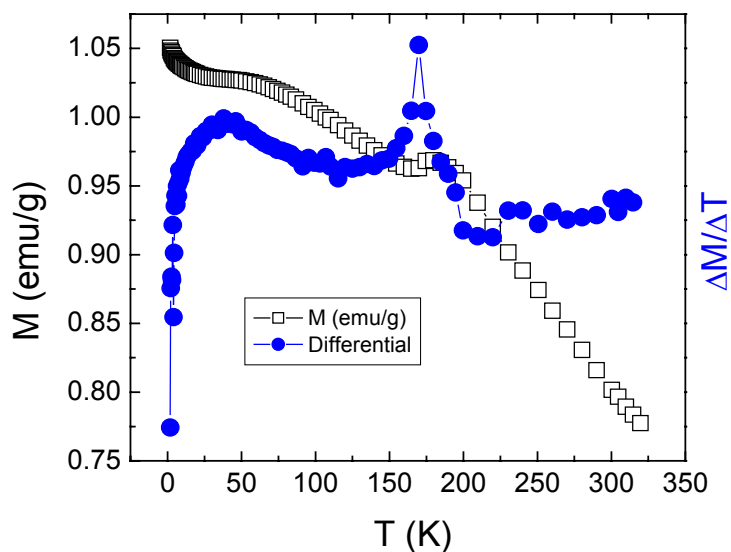


Figure 7. The M-T and $\Delta M/\Delta T$ curve of $\text{La}_{1/3}\text{Sr}_{2/3}\text{FeO}_{3-\delta}$ measured at a magnetic field of 5kOe.

The neutron diffraction data were analyzed by the FULLPROF code with separated phases for the crystal and magnetic structures respectively. Above 200K, there is no magnetic ordering, the crystal structure was refined in space group $R\bar{3}c$, $a=5.46$ and $c=13.36$ in the hexagonal setting. At low temperature, the magnetic structure was put in as an another phase and refined in space group P 1 that can give more flexibility to adjust the model. The unit cell of magnetic structure is the same as that of crystalline structure, which holds six iron atoms. The moments were in the basal plane. Figures 8(a) to 2(d) are neutron diffraction patterns at various temperatures for $\text{La}_{1/3}\text{Sr}_{2/3}\text{FeO}_{3-\delta}$.

517d:La1/3Sr2/3FeO3 11M 14K 1.4875

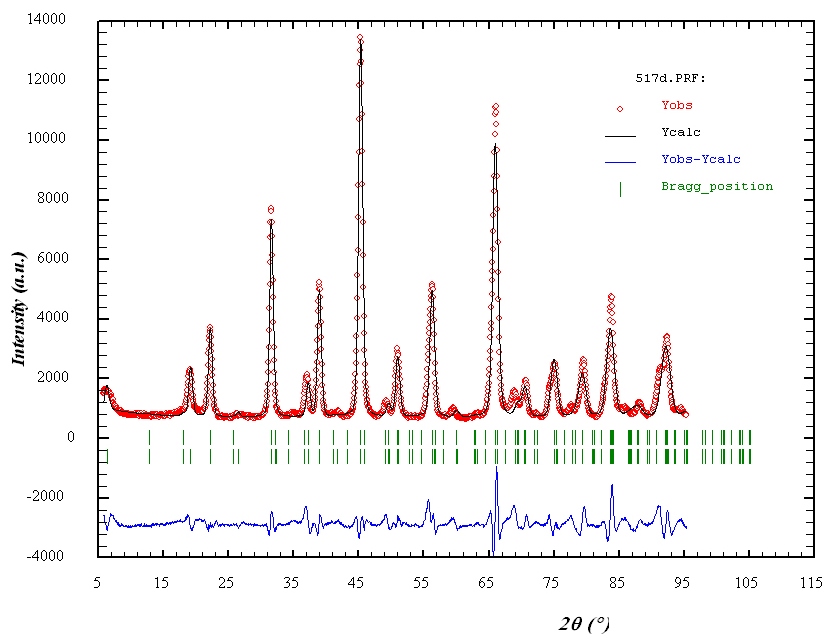


Figure 8a. Refinement of neutron data at 14K

(506d)La1/3Sr2/3FeO3 60K 5.4M

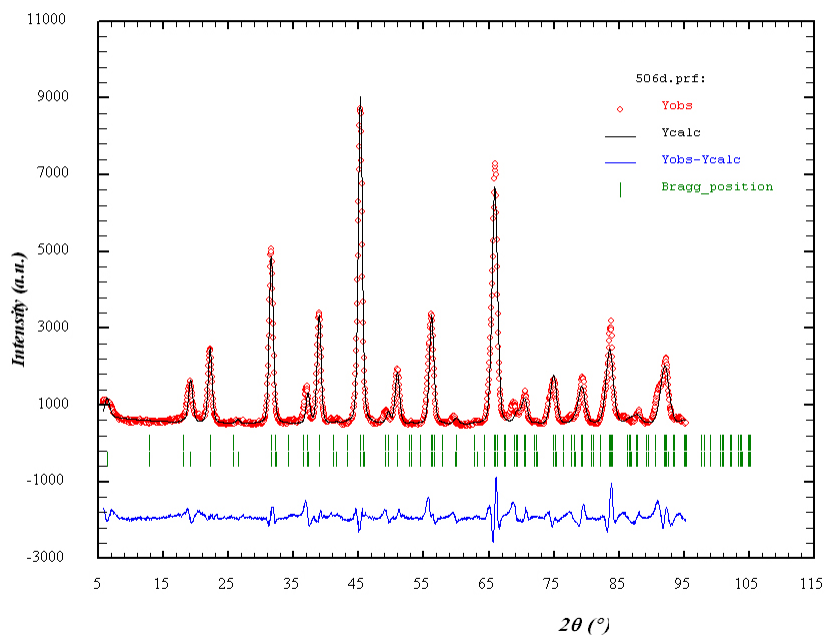


Figure 8b. Refinement of neutron data at 60K

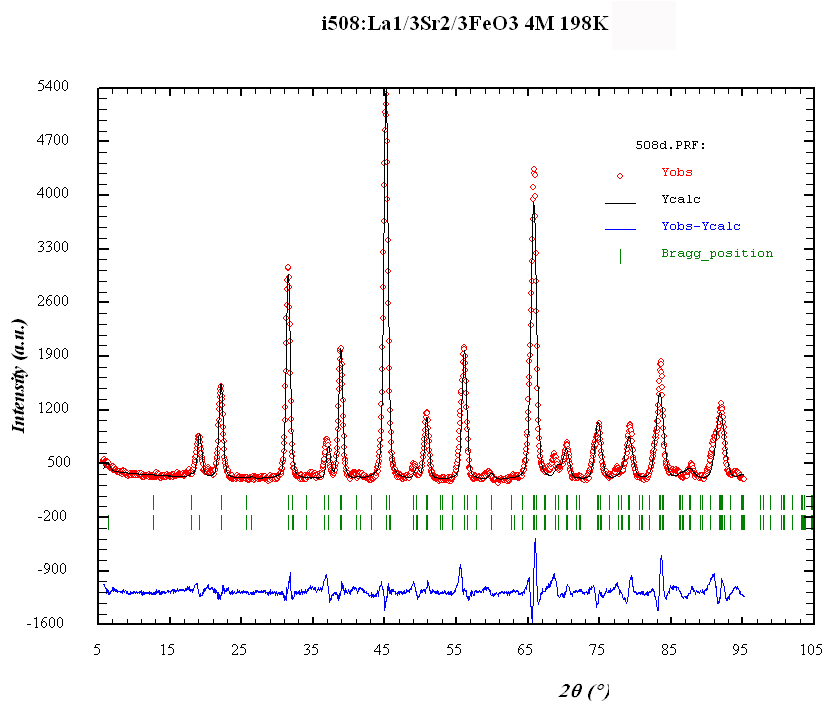


Figure 8c. Refinement of neutron data at 198K

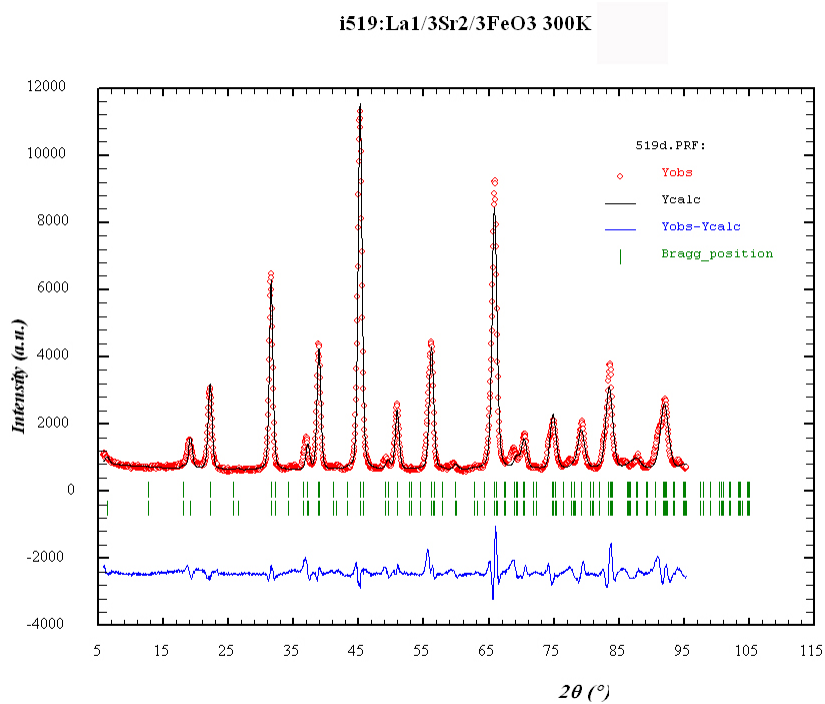


Figure 8d. Refinement of neutron data at 300K

The model used here was the same as Battle's³. However, the magnetic moments of Fe³⁺ and Fe⁵⁺, based on our refinement, are less than those of Battle's. If the moments are fixed to the values in Battle's paper, the refinement is shown in Figure 3. The calculated first peak, which was not shown in Battle's paper, mismatches significantly with neutron data in this study. It is possible that the omission of the first Bragg peak led to a false minimum in the refinement³.

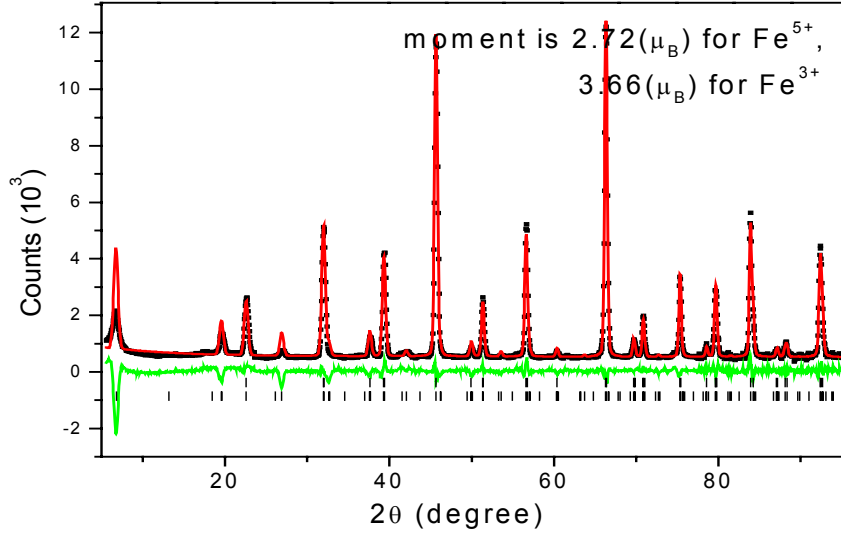


Figure 9 Refinement with Fe moments constrained to the values in reference 3.

Table 2 shows the dependence of crystal structure on the temperature. There is no noticeable structural change from 15K to 200K. The angles of both Fe-Fe-Fe and Fe-O-Fe are consistent to $\sim 2.6^\circ$ distortion for the $a^-a^-a^-$ tilt system according to the calculated results using our perovskite simulation program.

Table 2. Structural parameters at different temperature

Temp.	15K	80K	120K	160K	180K	200K
chi**2	5.2	2.11	2.25	2.25	1.98	2.01
a	5.4720(2)	5.4714(2)	5.4712(2)	5.4722(2)	5.4710(2)	5.4726(3)
c	13.3609(7)	13.365(1)	13.3640(9)	13.371(1)	13.368(1)0	13.377(1)
vol.	346.46(3)	346.50(4)	346.45(3)	346.75(3)	346.52(3)	346.97(5)
O, x	0.4781(4)	0.4773(5)	0.4771(4)	0.4773(4)	0.4781(4)	0.4793(4)
Fe-O-Fe	172.894	172.636	172.581	172.649	172.895	173.291
Fe-Fe-Fe	89.878	89.894	89.894	89.906	89.905	89.921
α (Rhom.)	59.930	59.939	59.939	59.945	59.945	59.954
Fe-O	1.93631	1.93665	1.93663	1.93711	1.93641	1.93685

Table 3 shows that the coupling between the moments of F^{5+} and F^{3+} is ferromagnetic; on the other hand, the coupling between the moments of F^{3+} and Fe^{3+} is antiferromagnetic.

Table 3 Temperature dependence of moments at different Fe-sites

Fe-site	15K	80K	120K	160K	180K	200K
(0,0,0)	1.367(57)	1.368(65)	1.313(63)	1.251(66)	1.144(76)	0
(1/3,2/3,1/6)	2.977(38)	2.887(43)	2.658(42)	2.216(47)	1.718(57)	0
(2/3,1/3,1/3)	-2.977(38)	-2.887(43)	-2.658(42)	-2.216(47)	-1.718(57)	0
(0,0,1/2)	-1.367(57)	-1.368(65)	-1.313(63)	-1.251(51)	-1.144(76)	0
(1/3,2/3,2/3)	-2.977(38)	-2.887(43)	-2.658(42)	-2.216(47)	-1.718(57)	0
(2/3,1/3,5/6)	2.977(38)	2.887(43)	2.658(42)	2.216(47)	1.718(57)	0

It was shown in Figure 10 that the magnetic moment of Fe^{3+} was about $3\mu_B$ at 15K, and decreased gradually to $1.7\mu_B$ at 180K. The magnetic moment of Fe^{5+} changes slightly from $1.4\mu_B$ at 15K to $1.2\mu_B$ at 180K. At 200K, moments of both of them drop suddenly to zero.

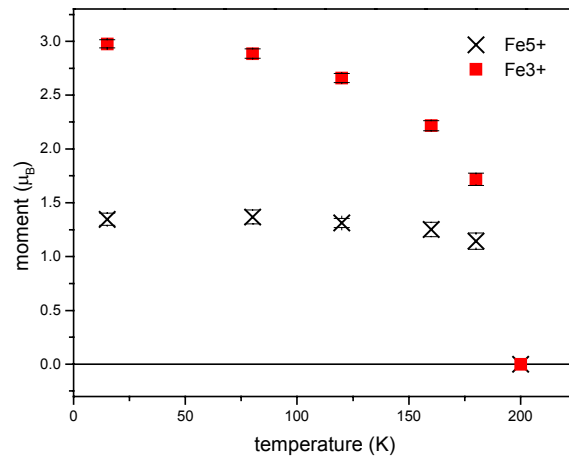


Figure 10. Magnetic moment (μ_B) of Fe^{5+} and Fe^{3+} .

The Mossbauer spectra of $La_{1/3}Sr_{2/3}FeO_{3-\delta}$ measured at different temperatures are shown in Figure 11. It is also evident that there is magnetic and charge ordering below 180K. The Mossbauer spectrum at 20K can be fitted with two hyperfine sextets with hyperfine fields of 47.3 and 26.9 telsa respectively, similar to the hyperfine fields of 45.1 and 25.9 telsa with which Battle fit his Mossbauer data³.

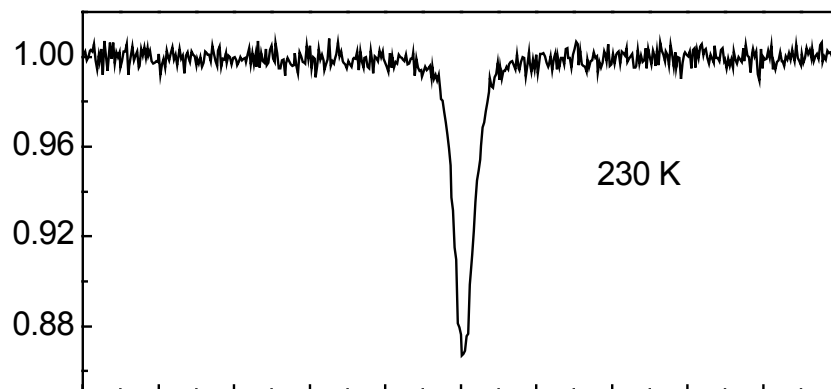


Figure 11a. Mossbauer spectra of $\text{La}_{1/3}\text{Sr}_{2/3}\text{FeO}_{3-\delta}$ measured at 230K

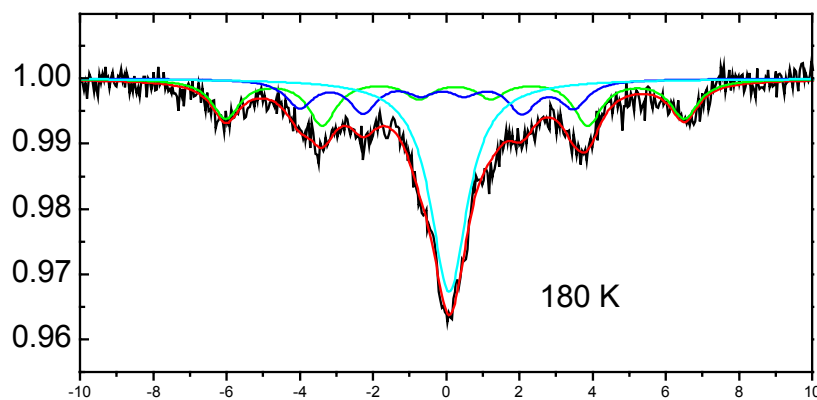


Figure 11b. Mossbauer spectra of $\text{La}_{1/3}\text{Sr}_{2/3}\text{FeO}_{3-\delta}$ measured at 180K

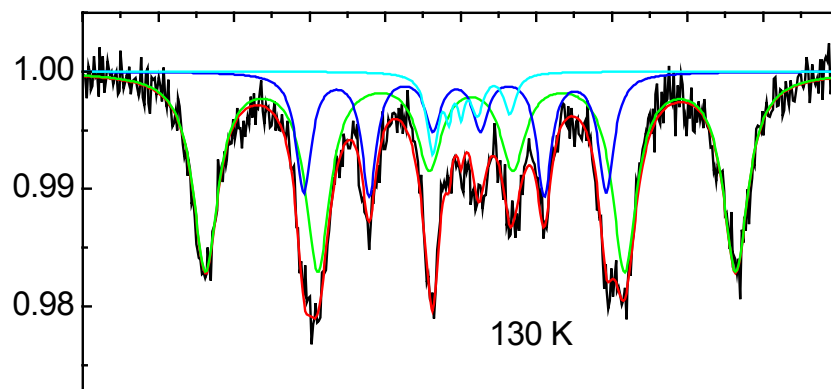


Figure 11c. Mossbauer spectra of $\text{La}_{1/3}\text{Sr}_{2/3}\text{FeO}_{3-\delta}$ measured at 130K

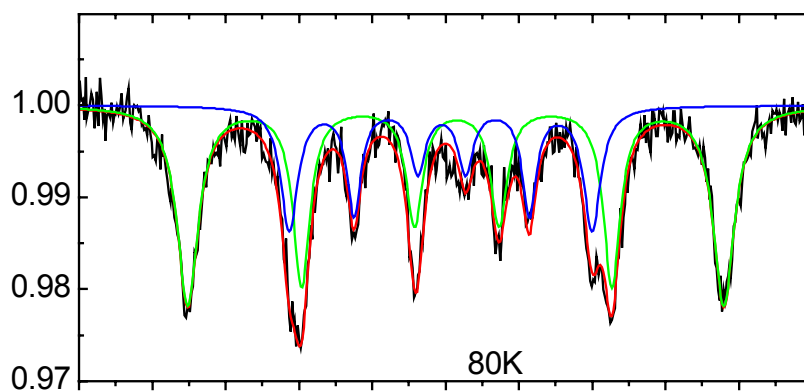


Figure 11d. Mossbauer spectra of $\text{La}_{1/3}\text{Sr}_{2/3}\text{FeO}_{3-\delta}$ measured at 80K

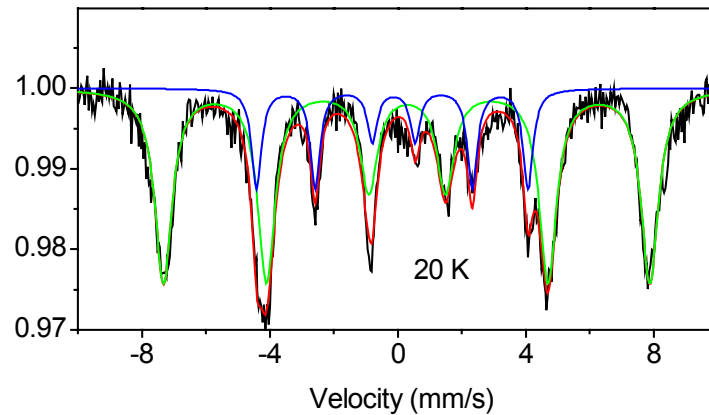


Figure 11d. Mossbauer spectra of $\text{La}_{1/3}\text{Sr}_{2/3}\text{FeO}_{3-\delta}$ measured at 20K

CONCLUSIONS

Based on our ND data, we can see that charge ordering appears at $< 189\text{K}$, and the charge ordering pattern is $\text{Fe}^{5+}\text{Fe}^{3+}\text{Fe}^{3+}\text{Fe}^{5+}\text{Fe}^{3+}\text{Fe}^{3+}$, which is consistent with Battle's model. However our 15K ND data show that the moments of Fe^{3+} and Fe^{5+} are $2.97 \mu_B$ and $1.36 \mu_B$, respectively, which are much less than the values of $3.6 \mu_B$ and $2.7 \mu_B$ in Battle's paper. Our ratio of refined moments appears to be consistent with the hyperfine fields calculated from the Mössbauer data. The sensitivity study of the moment to neutron data shows that the (0,0,1) peak is the most sensitive peak for moment, which was missing in Battle's data. It may explain why we get different moments.

FUTURE STUDIES:

Processing

1. Powder preparation: (1) the Pechini method; (2) Co-precipitation; and (3) Spray pyrolysis
2. Sintering: verifying the sintering temperature, time and atmosphere

Compositions

1. Ferrites: $\text{La}_{0.8}\text{Sr}_{0.2}\text{FeO}_{3-\delta}$ and $\text{La}_{0.4}\text{Sr}_{0.6}\text{FeO}_{3-\delta}$.
2. Others: $\text{La}_{0.8}\text{Sr}_{0.2}\text{Fe}_{0.8}\text{Co}_{0.2}\text{O}_{3-\delta}$ and $\text{La}_{0.6}\text{Sr}_{0.4}\text{Fe}_{0.8}\text{Co}_{0.2}\text{O}_{3-\delta}$.

Measurements:

1. Electrical Conductivity (σ_i and σ_e)
2. Mössbauer Spectroscopy
3. Neutron and x-ray diffraction
4. SQUID
5. Microstructure
6. SIMS (if available)

TASK 4: Assessment of Microstructure of the Membrane Materials to Evaluate the Effects of vacancy-Impurity Association, defect Clusters, and Vacancy Dopant Association on the Membrane Performance and Stability

Professor Nigel Browning, University of Illinois Chicago Circle

After the over one year break in funding for the UIC section of the research project, this quarter's research has focused on the training of a new graduate student to perform the analysis of membrane materials. Following the guidance that was received from the other project participants at the meeting in Rolla, the analysis will focus on the identification of precipitates at grain boundaries in fracture surfaces produced during testing at UAF. Of key importance in identifying the reasons for mechanical failure will be determining whether precipitation is a function of the deformation itself or produced in fracturing the surfaces. Initial analysis during this quarter's research has determined mechanisms of specimen preparation that will permit grain boundaries to be analyzed. The first quarter of 2003 will be spent performing initial analyses in the microscope to study the composition and distribution of precipitates at grain boundaries.

Task 5: Measurement of Surface Activation/Reaction rates in Ion Transport Membranes using Isotope Tracer and Transient Kinetic Techniques.

Prof. Alan Jacobson, University of Houston/University of Toronto

University of Houston

Conductivity and Thermodynamic Studies

We have continued to investigate the thermodynamic properties (stability and phase separation behavior) and total conductivity of prototype membrane materials. The data are needed together with the kinetic information to develop a complete model for the membrane transport. In previous studies, we have shown that iron based perovskite oxides show phase separation at intermediate partial pressures of oxygen, $-11 < \log pO_2 < -5$ at temperatures below 900 °C.

In previous measurements, we have measured the pO_2 dependence of the stoichiometry of $SrFeO_{3-x}$ in the temperature range $750\text{ °C} \leq T \leq 1040\text{ °C}$. Data were acquired manually both on increasing and decreasing pO_2 in order to confirm that the system had reached equilibrium. Our study showed that in that phase separation between perovskite and Brownmillerite phases is very slow and that very long equilibration times are necessary in order to obtain reliable data. As an example, the results obtained at 800 °C are shown in Figure 12. A clear discrepancy in the data at $pO_2 = \sim 10^{-7}$ atm is apparent at the phase boundary between perovskite and Brownmillerite.

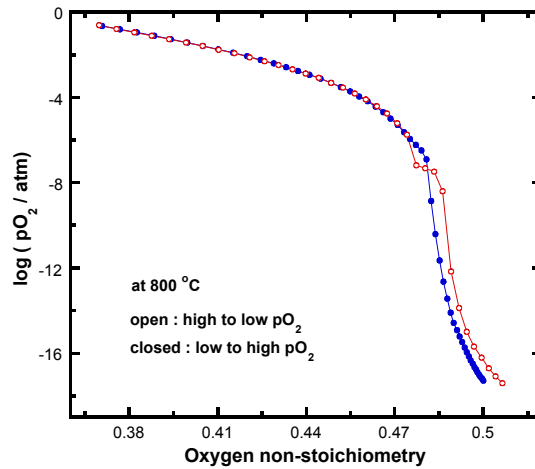


Figure 12. The effect of the low temperature phase separation on the 800 °C isotherm.

In the last quarter, we have extended the detailed characterization of $SrFeO_{3-x}$ to include measurements of the conductivity data. Recently Kozhevnikov *et al.* (1) measured the electrical conductivity and the Seebeck coefficient of $SrFeO_{3-x}$ in the temperature range $700 \geq T \geq 950\text{ °C}$ and at $0.3 \geq pO_2 \geq 10^{-18}$ atm. The results they obtained are shown in Figure 13 as a log-log plot

of conductivity versus pO_2 from 700 to 950 °C at 50 °C increments. The data show the expected p and n type behaviour at high and low oxygen partial pressures, respectively. The $\pm 1/4$ dependence is expected from a simple defect model with doubly ionized defects. Surprisingly, a pronounced discontinuity is observed in the conductivity at pO_2 values below 10^{-4} atm. A plateau is observed over a wide pO_2 range at 700 °C that decreases in width as the temperature is raised. Similar discontinuities were also observed in thermopower measurements. The same group have also measured several gallium substituted compositions and obtained comparable results. The measurements were made in one direction only with a criterion for equilibrium that the conductivity changed by less than 0.0005 S/min.

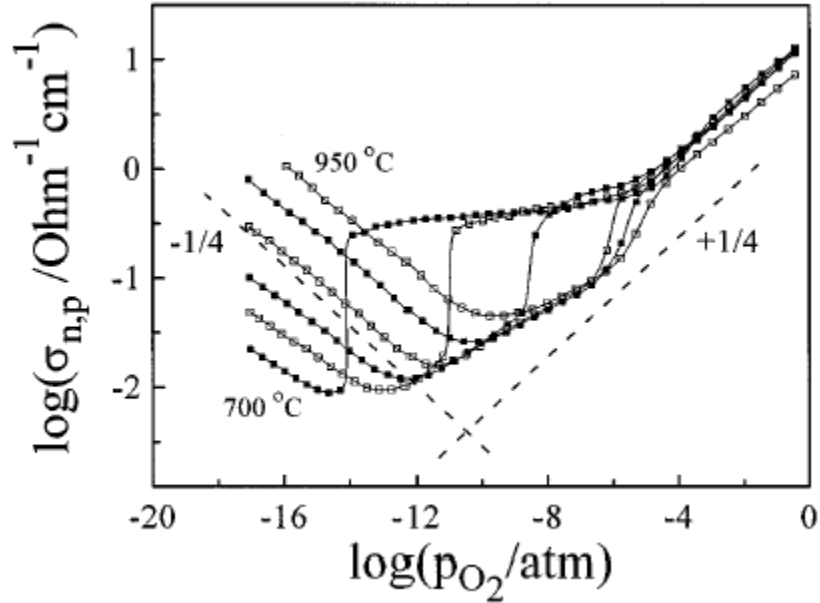


Figure 13. Conductivity isotherms for $SrFeO_{3-x}$ as a function of $\log(pO_2)$ taken from reference (1)

The results obtained by Kozhevnikov *et al.* (1) are surprising and not consistent with the data that we have obtained previously for $La_{0.2}Sr_{0.8}Fe_{0.8}Cr_{0.2}O_{3-x}$. Consequently, we have repeated the measurements using our own cell design. Measurements were made by the four probe technique using the cell design that we have described in previous reports that uses a YSZ pump to control the oxygen partial pressure and a YSZ sensor. The measurements were made using a lock-in amplifier in order to minimize the applied current and to avoid problems with pO_2 gradients inside the cell. In the initial experiments, Pt leads were used but problems were observed at very low oxygen partial pressures due to reaction of Pt with $SrFeO_{3-x}$ as illustrated by the results shown in Figure 14a. The filled circles correspond to measurements made with decreasing partial pressure of oxygen whereas the data represented by the open circles were obtained by first pumping the cell down to $pO_2 = \sim 10^{-11}$ atm and then increasing pO_2 . A significant discrepancy in the conductivity values observed below 10^{-8} atm, which we attribute to problems with the voltage probes. Subsequent experiments used Pt13%Rh voltage and current leads to avoid the problem.

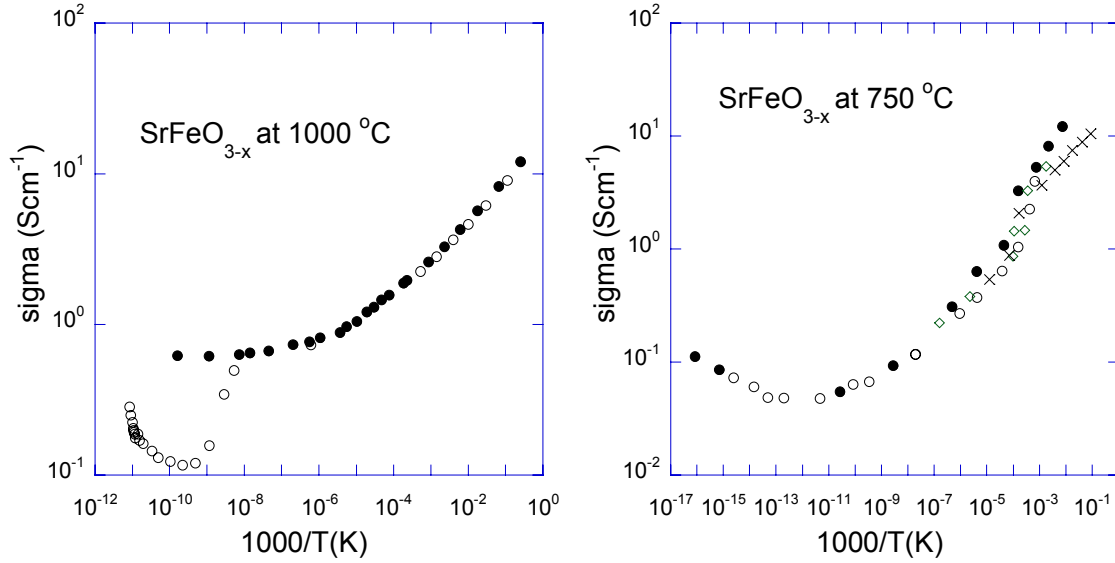


Figure 14 a) Conductivity of SrFeO_{3-x} at 1000 °C, filled and open circles represent measurements made on decreasing and increasing $p\text{O}_2$, respectively; b) Conductivity of SrFeO_{3-x} at 750 °C, the filled circles correspond to measurements from high to low $p\text{O}_2$, data with the other symbols were obtained from low to high $p\text{O}_2$.

The results for 750 °C are shown in Figure 14b where the filled circles correspond to measurements from high to low $p\text{O}_2$, and the data with the other symbols were obtained from low to high $p\text{O}_2$. In general, the magnitude of the conductivity is closely similar to that found in previous measurements but the shape is quite different. The shape of our 750 °C isotherm most closely resembles the previous data obtained at 950 °C. The present results were obtained using a criterion for equilibrium of $\sim 5 \times 10^{-5} \text{ Smin}^{-1}$, an order of magnitude slower than that used by Kozhevnikov *et al.* (1), and show no evidence for the plateau reported previously. Even with long equilibration times, at 750 °C some scatter in the data is apparent in the region where phase separation occurs.

The results for 750 °C and 850 °C obtained below a partial pressure of 10^{-5} atm are shown in Figure 15. The data were fit to a model in which the conductivity dependence on oxygen partial pressure is represented by a pressure independent ionic component and $\pm 1/4$ dependences for the n and p branches according to $\sigma = \sigma_0 + A p\text{O}_2^{+1/4} + B p\text{O}_2^{-1/4}$. The data for the two temperatures were least squares fit to extract the constants and the results are compared with the data of (1) in Table 1. The agreement is generally satisfactory.

Table 4 Low Pressure Conductivity Parameters for SrFeO_{3-x}

	σ_0	A	B	Ref.
750 °C	0.033	8.07	7.8×10^{-6}	this work
	0.028	9.76	2.8×10^{-6}	1.
850 °C	0.136	18.33	2.9×10^{-5}	this work
	0.084	5.08	1.7×10^{-5}	1.

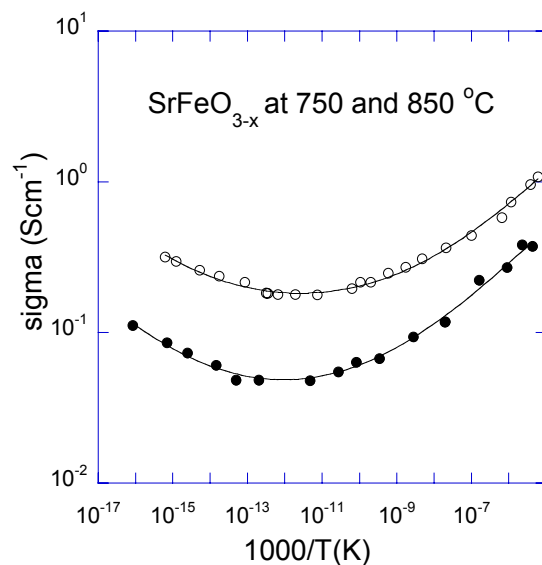


Figure 15 The low pressure conductivity of SrFeO_{3-x} at 750 and 850 °C.

In this quarter, we have synthesized a tubular ceramic sample of $\text{La}_{0.2}\text{Sr}_{0.8}\text{Fe}_{0.8}\text{Cr}_{0.2}\text{O}_{3-x}$ for use in the membrane reactor at UT (see Figure below).



Plans for next quarter.

We will complete the studies described above on the conductivity measurements for SrFeO_{3-x} . We will measure the partial pressure dependence of the stoichiometry of $\text{La}_{0.2}\text{Sr}_{0.8}\text{Fe}_{0.8}\text{Cr}_{0.2}\text{O}_{3-x}$ for which the present data are not satisfactory. In the next quarter, we will also synthesize additional tubular ceramics for use in the membrane reactor at UT.

Reference

1. V. L. Kozhevnikov, I. A. Leonidov, M. V. Patrakeev, E. B. Mitberg, K. R. Poeppelmeier, *Journal of Solid State Chem.* 158 (2000) 320.

Isotope Transient Studies of Oxygen Permeation Through a Dense $\text{La}_{0.6}\text{Sr}_{0.4}\text{Co}_{0.2}\text{Fe}_{0.8}\text{O}_{3-\delta}$ Membrane

Isotope transients ($^{16}\text{O}_2$ - $^{18}\text{O}_2$) were performed on a tubular (6mm o.d., 1 mm wall thickness) $\text{La}_{0.6}\text{Sr}_{0.4}\text{Co}_{0.2}\text{Fe}_{0.8}\text{O}_{3-\delta}$ (LSCF-6428) oxygen perm-selective membrane operating at steady state at temperatures between 1023K and 1123K. An $^{18}\text{O}_2$ isotope pulse was applied to the “air” ($20\%\text{O}_2$:Ar) side of the membrane while maintaining a constant $p\text{O}_2$. The isotopic composition of the oxygen permeate was analyzed on the delivery side, swept with helium, to reveal the residence time distribution of oxygen in the membrane under steady state transport. The resulting isotope transient allows the unambiguous separation of surface and bulk resistances to oxygen permeation under steady state conditions, a separation not possible by permeation measurements alone. The resulting transients show that both surface exchange and bulk transport resistances contribute significantly to this membrane performance. A dispersion flow model was fit to the data to provide values of the forward and reverse surface exchange rate coefficients as well as the oxygen diffusion coefficients. Oxygen flux increased substantially with the flow rate of sweeping gas, slightly with the flow rate of air. Evaluation of the transients with different sweep rates allows an unambiguous measure of the forward and reverse exchange rates of oxygen on the delivery side of the membrane. The values of the surface and bulk transport properties for this LSCF-6428 membrane are consistent with those measured for the same material by isotope infusion depth profiling (IEDP) experiments under gradientless conditions. For the conditions investigated, significant resistances were presented by bulk transport and the surface reactions.

Experimental:

Experimental setup As a reminder, the Figure 16 illustrates the configuration of the internals of the reactor. To minimize the undesired wall reactions, all parts which may contact gas mixture inside and outside of the perovskite membrane in the hot zone of the reactor are made of quartz except the gold seal. A bellows arrangement provides a constant force on the seals as the sample is heated and cooled. The temperature of furnace was controlled by a Omega Type I/32 PID temperature controller with an accuracy of ± 0.5 °C. Before and after each measurement, the temperature of the sample was measured by a K-type thermocouple as illustrated in Figure 16.

Oxygen isotope transient experiments. Synthesized air, $\text{O}_2:\text{N}_2 = 20:80$, was provided by Praxair Products Inc.. The ^{18}O -containing gas, $^{18}\text{O}_2:\text{Ar} = 20:80$, was supplied by Icon Isotopes. The ^{18}O isotope purity is 97%. The sample was equilibrated at the experimental conditions for at least 24 h in the natural abundance isotope version of the gas mixture. Following this equilibration the gas mixture O_2/N_2 in the air side of the membrane was switched to the ^{18}O containing mixture ($^{18}\text{O}_2/\text{Ar}$) and maintained for 15 min or 60 min. The flow rates of $^{18}\text{O}_2/\text{Ar}$ were 1-3 ml/min for the duration of isotope pulse to avoid depletion of the isotope oxygen, which depend on the experimental temperature and oxygen flux. A “pulse” of ^{18}O was then obtained in the oxygen-rich side. At the end of the pulse, the gas mixture was switched back to O_2/N_2 and kept the same experimental conditions as before for 4-6 days. The sweeping gas was analyzed with an on-line UTI Model 100C Quadrupole Mass Spectrometer (MS) through the experiment. The oxygen

fluxes were obtained simultaneously by an on-line GC analysis. Such experiments were carried out at various temperatures.

Results

In the previous report, we presented the dependence of oxygen flux on the He sweep rate (and therefore the oxygen partial pressure on the delivery side) and oxygen partial pressure on the air side. This dependence is not easily attributed to either surface or bulk resistances due to the coupling of the gradients involved. The section on modeling describes this aspect in more detail.

Figure 17 shows the results of isotopic transients. The shapes of the transients reveal the distribution of gradients in the membrane. This is illustrated by the model calculations below.

Modeling

We have used a 1-D constant properties computer based finite element model shown schematically in Figure 18. The model makes the following assumptions:

- (1) The surface activation on the air side is partly reversible. This determines the amount of isotope that enters the membrane during the pulse and that “back-exchanges” after the ^{18}O isotope is switched off.
- (2) Diffusional broadening of the isotope pulse as it transients the bulk is assumed to occur with a constant diffusion coefficient and that the oxygen stoichiometry is constant across the membrane.
- (3) The surface reaction on the delivery side is also reversible, but this reversibility has no effect on the oxygen isotope with a helium sweep because the only oxygen on the delivery side arises from the membrane and the isotope composition in the gas on the delivery side will always be the same as the surface concentration.

The model was used to fit the measured transients in a trial and error manner. Figures 19 and 20 shows how the relative transport parameters influence the observed transient. In Figure 19 constant surface activation rates and oxygen flux were assumed and the oxygen diffusion coefficient varied. The shapes of the transients change from a delta function if the diffusion coefficient is extremely small to an exponential decrease for very large values of the diffusion coefficient. Since the diffusion coefficient is related to the mobility, narrower transients should arise from larger activity gradients across the membrane. Figure 20 shows the changes that result from changes in the reversibility of the surface reaction on the air side. Again, the erosion of the pulse by back exchange changes the shape of the transient in. This sensitivity allows the values

of the surface exchange coefficients and the bulk diffusion coefficient in the membrane under operation.

Model fits to the data

Figure 21 shows the fit to the 60 minute isotope pulse at 800°C. Similar fits were obtained to the other transients. The circles in Figure 22 show the diffusion coefficients obtained from the model fits to our transient data. The diamond is the value of D^* measured by Kilner and Lane in IEDP experiments and the line is a correlation obtained at the University of Houston by Jacobson and Wang using conductivity relaxation techniques. The values measured in these experiments under an operating gradient are in very good agreement with values obtained under no chemical gradient (IEDP) and modest gradients (conductivity relaxation).

Figure 23 shows the value of the surface activation rate coefficient measured in these experiments (triangles, pointing up for reverse process and down for the forward activation rate. These are compared with the values obtained in IEDP and conductivity relaxation experiments. These are also in relatively good agreement, though the conductivity relaxation experiment should actually measure be the net of the forward and reverse processes.

These experiments have shown the value of the isotope transient technique and the connection of the operating membrane to the transport coefficients measured under gradientless conditions. The conditions used here also produce relatively modest oxygen activity gradients across the membrane and under these conditions such agreement is not unexpected. The results of this technique under large oxygen gradients will be much more revealing.

Plans

We will analyze the current data base to extract the oxygen potential profile across the membrane during these experiments. We will also perform transients on $\text{La}_{0.6}\text{Sr}_{0.4}\text{Co}_{0.2}\text{Fe}_{0.8}\text{O}_{3-\delta}$ with varying He sweep rates and oxygen partial pressures. This should vary the potential drop across the bulk and provide further tests of the sensitivity of the model. With the new $\text{La}_{0.2}\text{Sr}_{0.8}\text{Cr}_{0.2}\text{Fe}_{0.8}\text{O}_{3-\delta}$ shown above, we will also begin an examination of membranes under syngas generation conditions with large oxygen activity gradients.

FIGURES:

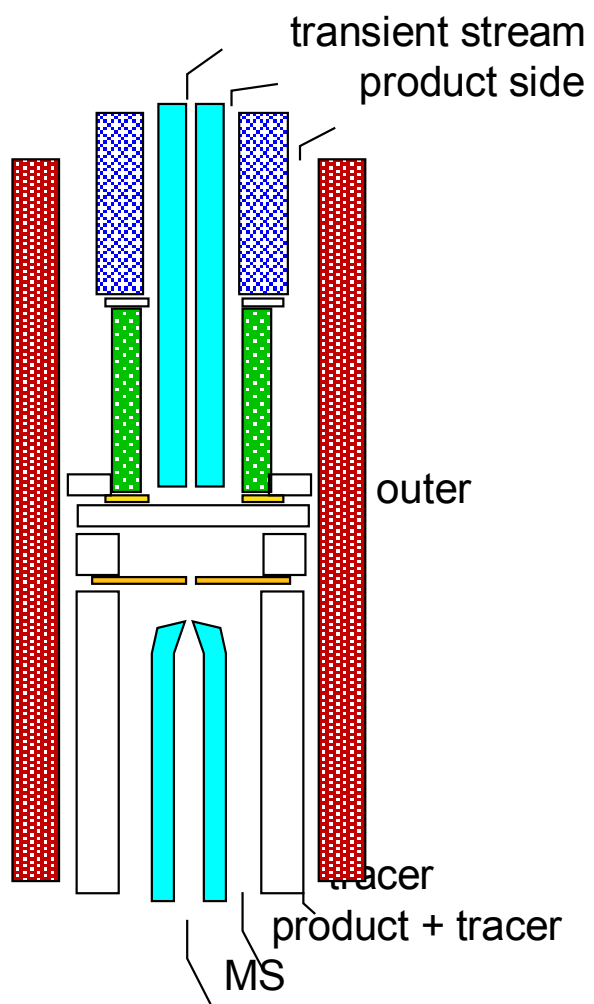


Figure 16: Schematic of the isotope transient experimental reactor.

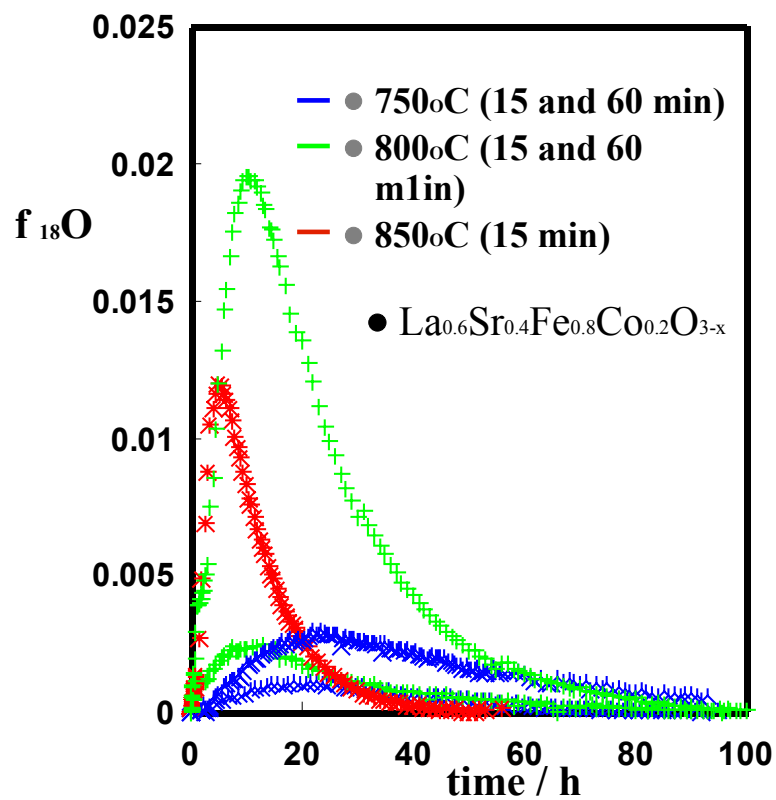
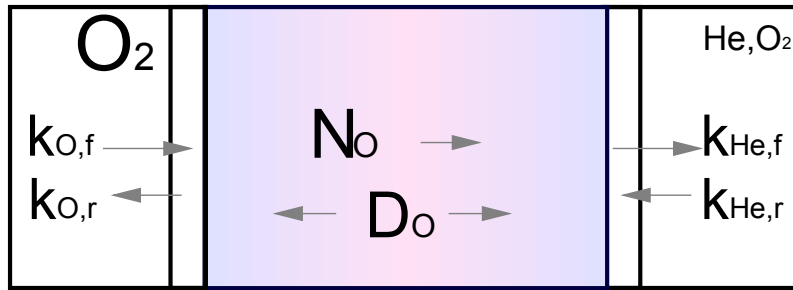


Figure 17: Isotope transients on operating LSFCE membranes at the conditions indicated. The numbers in parenthesis are the duration of the isotopic pulse.



- Reversibility at air side
- Related to k^* (IEDP)
- Diffusional mixing under gradient
- Related to D^* (IEDP)
- Cannot measure reversibility at sweep side (unless some oxygen fed)

Figure 18: schematic of the parameters in the 1-D model described in the text.

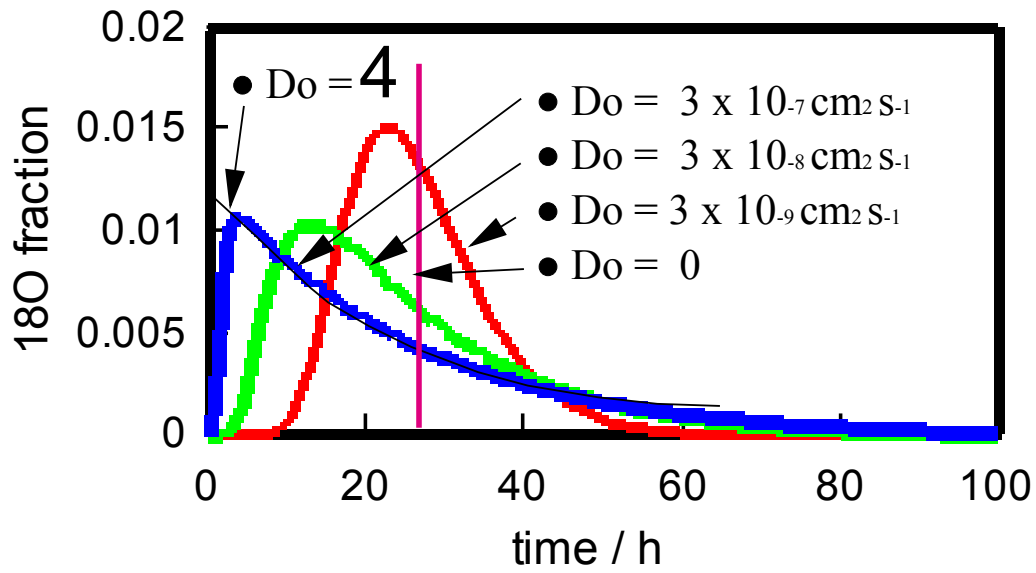


Figure 19: Model outputs for hypothetical operating conditions (flux, surface activation rates) and different oxygen diffusion coefficients.

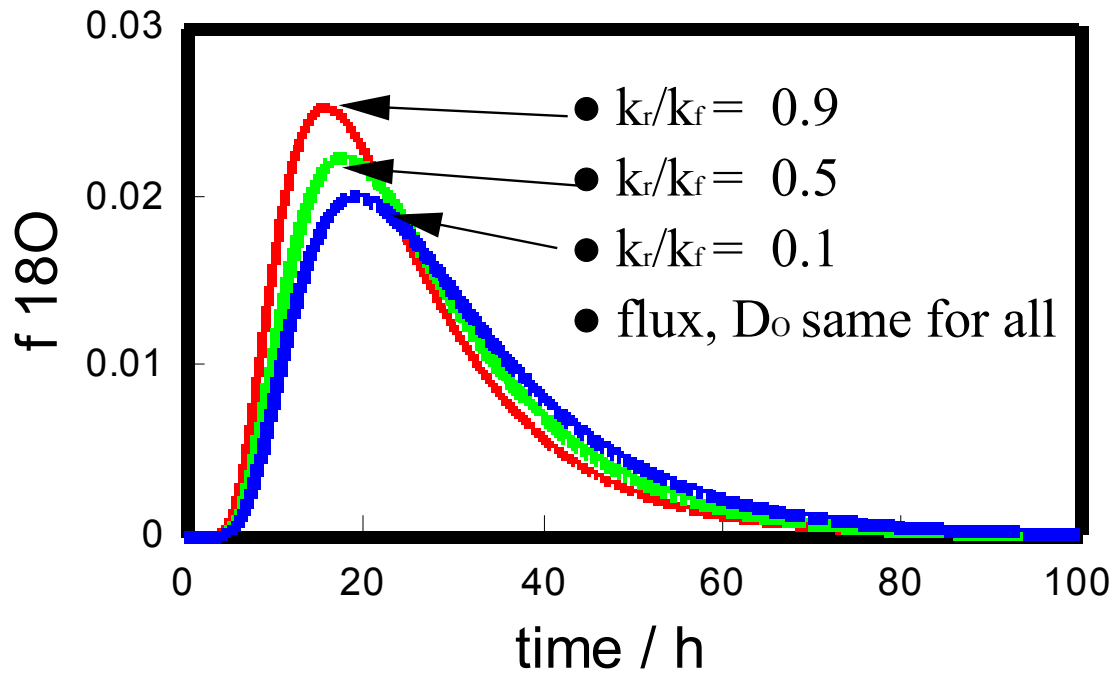


Figure 20: Model outputs for hypothetical operating conditions (flux, diffusion coefficient) and different degrees of reversibility of the surface activation rate.

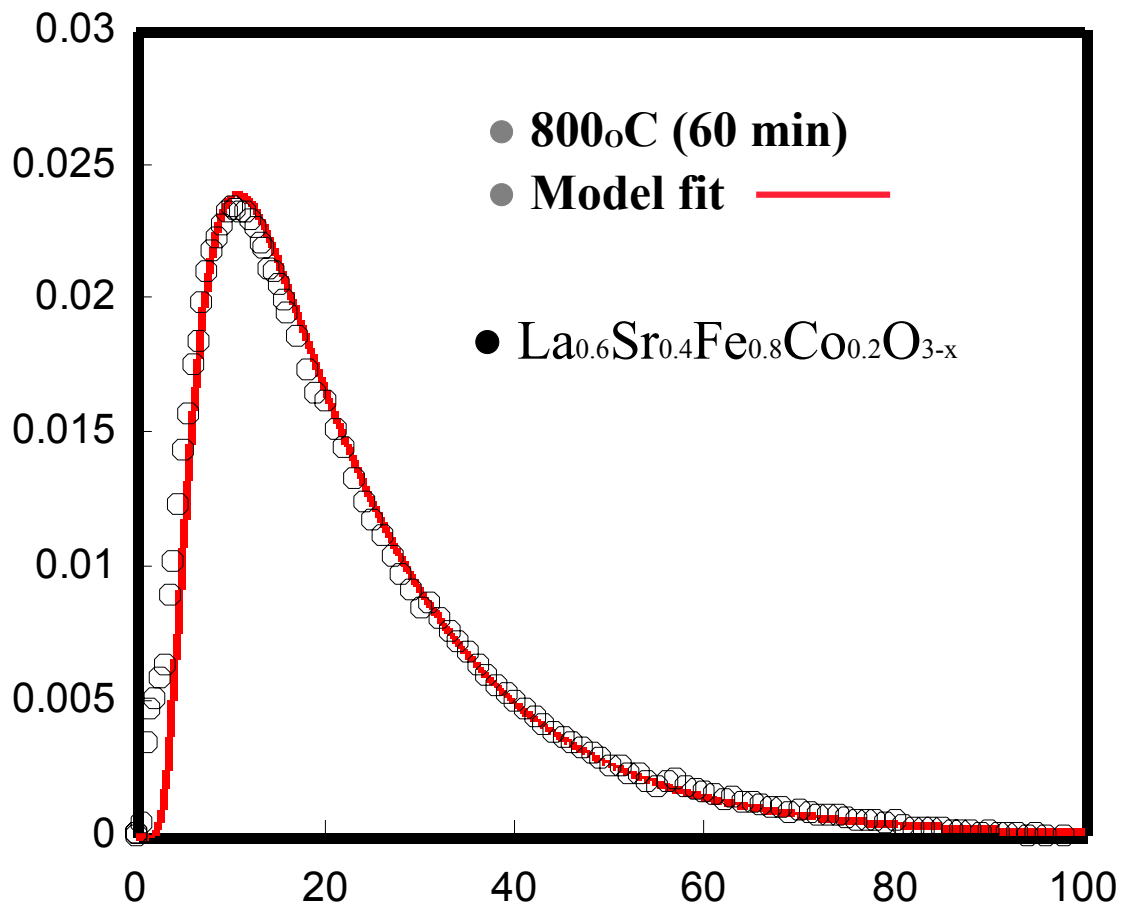


Figure 21: Fit of the isotope transient at 800C and a 60 minute pulse with the 1-D model.

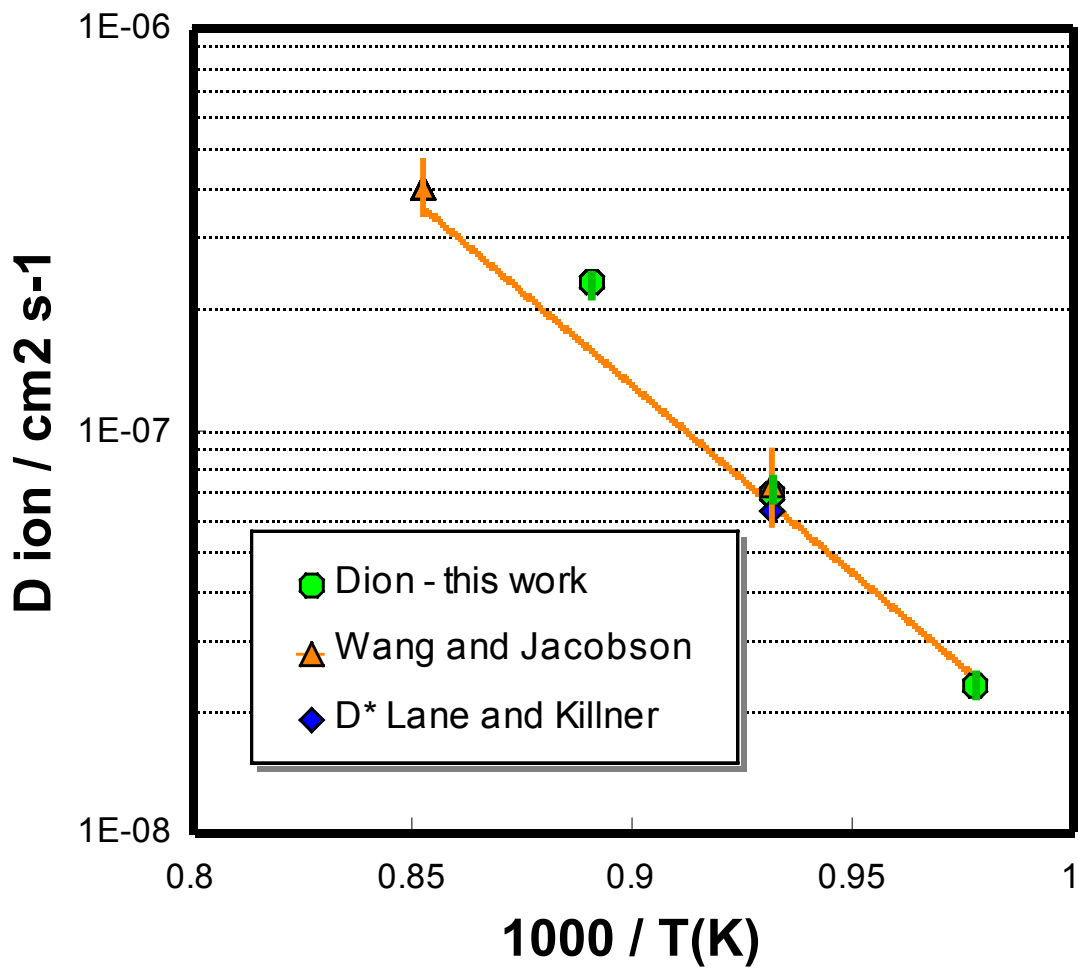


Figure 22: Comparison of oxygen diffusion coefficients measured in these experiments with values obtained in IEDP and conductivity relaxation experiments. See text for discussion.

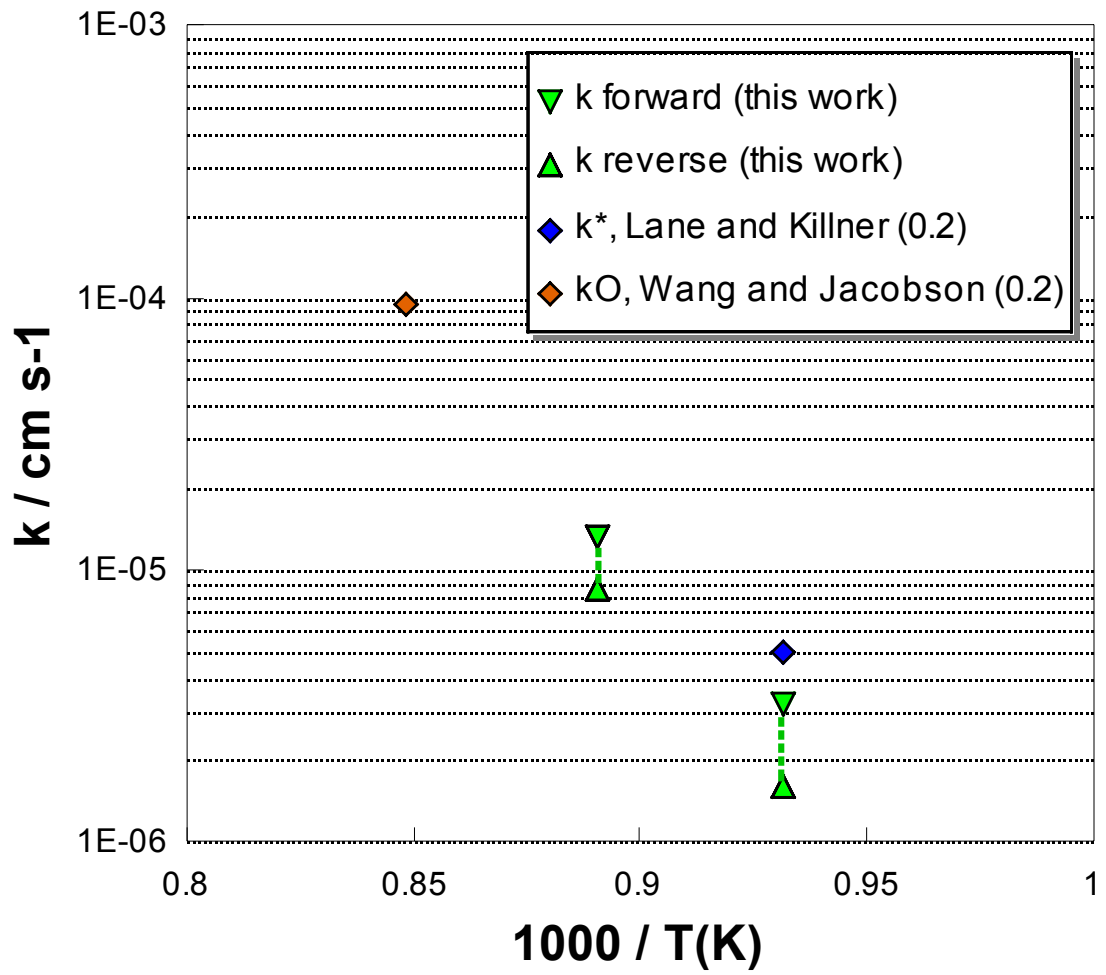


Figure 23: Comparison of air side oxygen activation rates measured in these experiments with values obtained in IEDP and conductivity relaxation experiments. See text for discussion.